UNIVERSITY OF BIRMINGHAM

University of Birmingham Research at Birmingham

Developing a detailed multi-body dynamic model of a turnout based on its finite element model

Shih, Jou Yi; Ambur, Ramakrishnan; Dixon, Roger

Document Version
Publisher's PDF, also known as Version of record

[Link to publication on Research at Birmingham portal](#)

Developing a detailed multi-body dynamic model of a turnout based on its finite element model

Jou-Yi Shih, Ramakrishnan Ambur & Roger Dixon

Published online: 04 Oct 2021.

Submit your article to this journal ⬚

Article views: 218

View related articles ⬚

View Crossmark data ⬚

IA**VSD**

Taylor & Francis
Taylor & Francis Group

Developing a detailed multi-body dynamic model of a turnout based on its finite element model

Jou-Yi Shih 🆔[a,b], Ramakrishnan Ambur 🆔[a] and Roger Dixon 🆔[a]

[a]Birmingham Centre for Railway Research and Education, University of Birmingham, Birmingham, UK; [b]ZynaMic Engineering AB, Stockholm, Sweden

ABSTRACT

This paper proposes a three-layered co-running track model for predicting and analysing the dynamic behaviour of railway turnouts during the passage of trains. It is a multi-body dynamic model with space-dependent track parameters. The method is demonstrated by applying a UIC60-760-1:15 turnout (with curve radius 760 m and turnout angle 1:15). Equivalent track properties are introduced, based on the turnout track flexibility, and the rail receptance and impact force results are compared with the results from a finite element (FE) model. The validation results show a good agreement with those of the FE model, but with far less computational expense in terms of power and time. The new model is found to capture the dominant dynamic behaviour of the turnout across all frequencies up to 2000 Hz. The results have drawn that consideration of higher frequencies is important due to the nature of dynamic forces affecting the crossing region and high-speed cases.

1. Introduction

Turnouts, which are also called switches and crossings (S&Cs), are among the most problematic assets in the railway system. They generally result in high maintenance and replacement costs due to poor system performance. Therefore, there is a need for engineers to understand the mechanical behaviour of turnouts, during the passage of trains to investigate potential improvements to the existing systems; numerical simulation has been widely used for this purpose.

To capture the complete system performance, it is important to consider the vehicle/turnout interaction dynamics. Multi-body simulation (MBS) has been widely used for modelling vehicle/track interaction dynamics and for vehicle/turnout dynamics [1]. A co-running track approach is used for the MBS model, which places a simplified multi-body track model under the wheelset which moves with the vehicle (with the same velocity). The track model, usually with only a few degrees of freedoms (dofs), represents the track components, such as the rail and sleepers. Alternative approaches use finite element (FE) models, which provide a complete track model that is able to capture the actual track flexibility, which is important for modelling vehicle/track interaction dynamics [2,3], especially

---

CONTACT Jou-Yi Shih ✉ jouyishih@gmail.com

for capturing results at higher frequencies [4]. However, simulation time for such FE models is far greater than that for MBS models [2], due to their computational complexity; hence, often they are inefficient to use.

Some authors extend the use of a MBS' numerical approach to capture the track flexibility, and different types of MBS track model have been presented and discussed in [5]. The track parameters for MBS co-running track model can be calibrated through the rail receptance measurement [6,7], or can be tuned by fitting the rail receptance results from the FE model [8], or can be simply calculated based on an infinite beam on elastic foundations [4,9]. The track flexibility for a turnout is even more difficult to estimate than that for the plain track. The rail cross-sections and sleeper lengths change along the turnout and consequently change the structural dynamic characteristics. Consequently, the MBS co-running track parameters for the whole turnout, based on calibration at only one location, are not sufficiently accurate [6]. Although space-dependent parameters of a co-running track model were used to consider the complete turnout flexibility by [7,8], the results are only valid up to 200 Hz.

The aim of the study is to propose a strategy to derive equivalent track properties for a co-running MBS track model inspired by [4,9], which can capture the dynamic behaviour of the whole flexible turnout up to 2000 Hz. It is important to consider higher frequency for vehicle/turnout interaction modelling because significant impacts, which cause rail damage, occur at higher frequency range and this frequency tends to increase when the train speed increases.

The flexible turnout model, from which the parameters of MBS models are derived, is explained in section 2. Results from two MBS models, which contain two and three layers, are compared in this paper. The layout of the two-layered MBS model is the same as proposed in [1]. The first (bottom most) layer of the co-running track model contains the equivalent properties of the sleeper and the ballast. The second layer contains those of rails and the rail pads. In the three-layered model, the third layer does not represent any physical components, but rather a virtual spring-mass-damper system to better approximate the higher frequency responses. These models, along with the method to calculate the parameters, are described in section 3. The rail receptance results from a high fidelity FE turnout model is used for validating the results of the newly proposed method. Section 4 shows the results from vehicle/track interaction with these co-running track models, comparing them with the results of co-simulation of MBS vehicle and FE track structure model [2].

2. The 3-dimensional finite element model of the turnout

Figure 1(a) shows the schematic of the turnout, whose finite element model is described in detail in [2]. The objective is to parameterise an MBS model based on this structural model. Track static stiffness is calculated first to investigate the overall turnout characteristics. The static stiffness at every sleeper location is calculated based on the rail receptance at 1 Hz from the FE turnout model. The plots in Figure 1(b,c) show the vertical and lateral static stiffnesses, respectively, along the turnout calculated from the FE model.

As shown in Figure 1(b), the vertical stiffness for the stock rail (outer rail) remains the same throughout the turnout. The vertical stiffness for the switch rail at the toe is lower than the stock rail but increases gradually ($x < 44.29$m). The rail pad stiffness of the
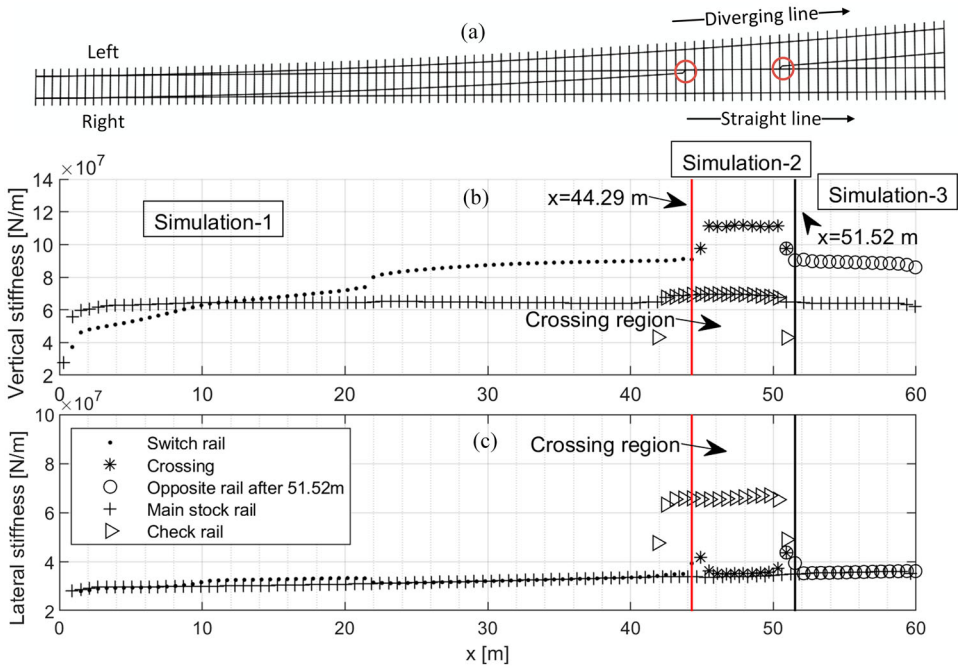
Figure 1. (a) Schematic of the turnout; (b) static track stiffness of the turnout in vertical; (c) lateral directions.

crossing nose (44.29m < x < 51.52m) is much higher, after which the stiffness decreases (x > 51.52m).

The overall lateral stiffnesses are equal for all rails along the turnout, except check rails, as shown in Figure 1(c). This is due to the fact that the check rails are typically mounted on very stiff L-brackets in reality; therefore, much higher lateral rail pad stiffness is applied for the check rails. The lateral stiffness values increase gradually from the switch toe till the end of the turnout, as shown in Figure 1(c). Around 25% difference is found between the values at the beginning and end of the turnout for all rails. Some discontinuous points can be found near the crossing region, highlighted as red circles in Figure 1(a). This is due to the constraint elements used between the two rail elements in the FE model. Significant spring stiffness is applied to connect the two rails at the crossing region. Table 1 shows the summary of the values of various elements in the finite element model for the UIC60-760-1:15 turnout. Because the cross-section and thereby the mass of switch rail gradually builds from switch toe onwards, some of its values monotonically increase.

3. The co-running multi-body track model

Figure 2 shows the two-layered co-running track model used in [1]. To better capture the response at higher frequency, an extra dummy mass (m_0) is positioned above each rail mass ($m_{r1} - m_{r4}$) on the two-layered model to build a three-layered co-running MBS track model, as shown in Figure 3. Equivalent track properties for two-layered and three-layered co-running track models are derived based on the corresponding values of flexible turnout, as shown in Figure 1. The calculation of stiffness and damping properties are

Table 1. Track properties for the whole FE turnout.

Parameter	Stock	Switch	Crossing	Check	Units
Rail					
Rail mass density, ρ_r	7850	7850	7850	7850	kg/m^3
Rail Young's modulus, E_r	207×10^9	207×10^9	207×10^9	207×10^9	N/m^2
Rail shear constant, κ	0.4	0.4	0.4	0.4	
Rail area, A_r	0.0076668	0.0056262–0.009353	0.023	0.0076668	m^2
Rail second moment inertia in the vertical direction, $I_{r,z}$	3.03×10^{-5}	5.23×10^{-6}–3.03×10^{-5}	9.09×10^{-5}	3.03×10^{-5}	m^4
Rail second moment inertia in the transversal direction, $I_{r,y}$	5.13×10^{-6}	5.13×10^{-6}–7.45×10^{-6}	5.11×10^{-6}	5.13×10^{-6}	m^4
Sleeper					
Sleeper mass density, ρ_s	2400	2400	2400	2400	kg/m^3
Sleeper Young's modulus, E_s	37.5×10^9	37.5×10^9	37.5×10^9	37.5×10^9	N/m^2
Sleeper area, A_s	0.054824	0.054824	0.054824	0.054824	m^2
Sleeper second moment inertia in the vertical direction, I_s	224×10^{-6}	224×10^{-6}	224×10^{-6}	224×10^{-6}	m^4
Sleeper length, L_t	2.5	2.5	4.06	4.06	m
Stiffness and damping					
Vertical rail pad stiffness, $k_{p,z}$	120×10^6	120×10^6	120×10^6	120×10^6	N/m
Vertical rail pad damping, $c_{p,z}$	25×10^3	25×10^3	25×10^3	25×10^3	Ns/m
Lateral rail pad stiffness, $k_{p,y}$	25×10^6	25×10^6	25×10^6	120×10^6	N/m
Lateral rail pad damping, $c_{p,y}$	10×10^3	10×10^3	10×10^3	25×10^3	Ns/m
Sleeper spacing, L_s	0.6	0.6	0.6	0.6	m
Ballast vertical stiffness per unit length $s_{b,z}$	20×10^6	20×10^6	20×10^6	20×10^6	N/m^2
Ballast vertical damping per unit length $d_{b,z}$	200×10^3	200×10^3	200×10^3	200×10^3	Ns/m^2
Ballast lateral stiffness per unit length $s_{b,y}$	10×10^6	10×10^6	10×10^6	10×10^6	N/m^2
Ballast lateral damping per unit length $d_{b,y}$	100×10^3	100×10^3	100×10^3	100×10^3	Ns/m^2
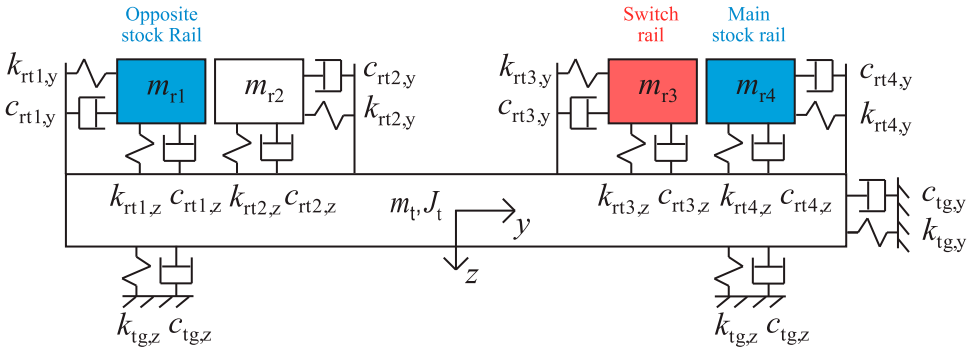
Figure 2. Two-layered co-running MBS track model [1].

shown in section 3.1 and the mass is shown in section 3.2. The two different track models are validated against the whole FE turnout model using rail receptance in section 3.3.

3.1. Equivalent stiffness and damping values

3.1.1. Parameters in the vertical direction

To capture the track flexibility, effective lengths for the rail and the sleeper should be determined. The effective length is the wavelength of the system when a unit point load is
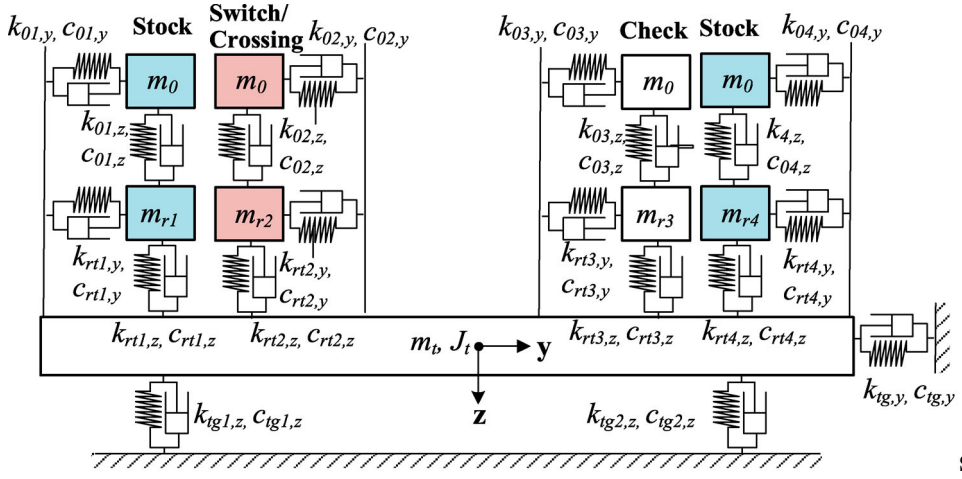
Figure 3. Three-layered co-running track model for the turnout.
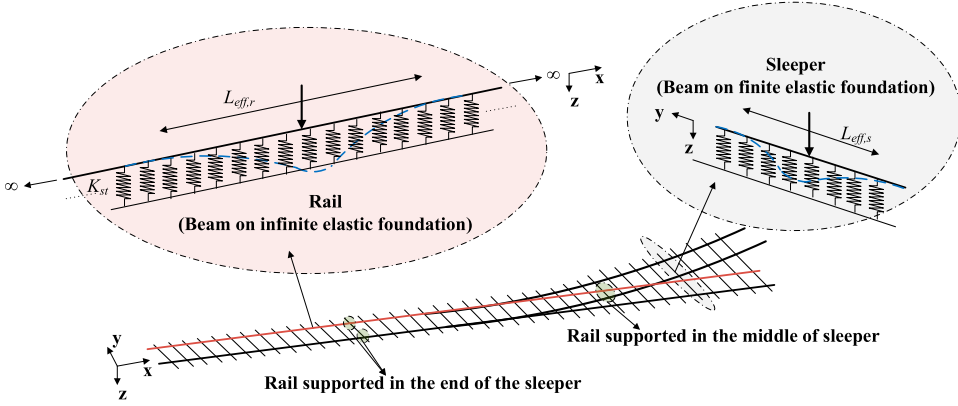
Figure 4. Effective lengths for the rail and the sleeper.

applied, as shown in Figure 4. To calculate them, the rails and sleepers are considered to be infinite and finite beams, respectively, on elastic foundation, as shown in Figure 4. Equations (1) and (5) show the formula to calculate the effective lengths of rail and sleeper, respectively. Their derivation, presented in the subsequent paragraphs, shows how these lengths are calculated separately for the rails supported in middle and edge of the sleeper by Equations (3), (4) respectively, and also the continuously varying support stiffness of rail by Equations (10) and (15).

The effective length for each rail on the turnout can be calculated by the static track stiffness (K_{st}) and the stiffness of an equivalent continuous support layer (k_s), as given in Equations (1) and (2), respectively [9].

$$L_{eff,r} = K_{st}/k_s \tag{1}$$

$$k_s = \frac{k_{p,z}k_{b,z}}{L_s(k_{p,z}+k_{b,z})}; K_{st} = 2\sqrt{2}(E_r I_{r,z})^{1/4}k_s^{3/4} \tag{2}$$

Here $k_{p,z}$ and $k_{b,z}$ are the rail pad and ballast vertical stiffnesses, respectively, in the flexible (FE) track model. L_s is the sleeper spacing, and $E_r I_{r,z}$ is the bending stiffness of the rail. In the FE model, the ballast vertical stiffness is defined as stiffness per unit length ($s_{b,z}$), as shown in Table 1. Therefore, equivalent $k_{b,z}$ values are calculated from Equations (3) and (4). An example of rails supported at the edges of the sleeper is the stock rails when a plain track is considered. Their equivalent stiffness can be calculated by dividing the total ballast stiffness by the total number of the supported rails, (i.e. for the plain track $n = 2$ and for the crossing region $n = 3$).

$$\text{Rail supported in the middle of sleeper (see Figure 4)} : k_{b,z} = s_{b,z} L_{eff,s} \qquad (3)$$

$$\text{Rail supported in the edge of sleeper (see Figure 4)} : k_{b,z} = s_{b,z} L_t / n \qquad (4)$$

The effective length for sleeper $L_{eff,s}$ is calculated as

$$L_{eff,s} = \frac{2}{L_t \left(\frac{s_{b,z}}{4 E_s I_s} \right)^{1/4}} \qquad (5)$$

where L_t is the length of the sleeper and $E_s I_s$ is the vertical bending stiffness of the sleeper. Equation (5) takes the sleeper static stiffness as the response of a finite beam on elastic foundation into account. For rails supported in the middle of the sleeper, it is important to consider this factor.

Finally, the values of stiffness and damping in the vertical direction for the three-layer and two-layered co-running track models can be obtained from Equations (6–9).

$$\text{Rail pad vertical stiffness} : k_{rtj,z} = k_{p,z} L_{eff,r} / L_s \quad (j = 1 - 4) \qquad (6)$$

$$\text{Rail pad vertical damping} : c_{rtj,z} = c_{p,z} L_{eff,r} / L_s \quad (j = 1 - 4) \qquad (7)$$

$$\text{Ballast vertical stiffness} : k_{tgj,z} = k_{b,z} L_{eff,r} / L_s \quad (j = 1 - 2) \qquad (8)$$

$$\text{Ballast vertical damping} : c_{tgj,z} = c_{b,z} L_{eff,r} / L_s \quad (j = 1 - 2) \qquad (9)$$

Different effective lengths for rail at different regions should be calculated for stock, check, and crossing rail based on the parameters given in Table 1. The switch rail cannot be considered as an infinite beam, as its cross-section changes along the turnout until about 22 m from the switch toe. Therefore, the vertical support stiffness of the switch rail is estimated based on the parameters derived for the stock rail and multiplied with a factor Δ_z. This factor, as given in Equation (11), is the ratio of vertical support stiffness between the switch rail and stock rail in the flexible turnout model. From the values of the FE turnout model, the vertical stiffness of the switch rail is approximated by a quadratic equation, as given in Equation (10).

$$K_{sw} = -2.4 * 10^4 x^2 + 2.2 * 10^6 x + 4.2 * 10^7 \qquad (10)$$

$$\Delta_z = K_{sw} / K_{st} \qquad (11)$$

Here K_{st} is the stock rail continuous support stiffness, which is approximately 6.4×10^7 N/m based on Equation (2). Between 22 m from the switch toe until the crossing region, the support stiffness of the switch rail is maintained as a constant value similar to the trend shown in Figure 1(b) for the flexible model.

To achieve a better approximation to the high-frequency behaviour of the track model, a three-layered track model is developed, as mentioned earlier. For the extra layer, the mass, stiffness ($k_{0j,z}$) and damping ($c_{0j,z}$) in the vertical direction should be determined. The value of stiffness ($k_{0j,z}$), which is modelled in parallel to the damping, is considered to be equal to that of the rail pad stiffnesses in the second layer. The dummy mass (m_0) is given a value of 2.5 kg. According to [9], additional damping can be added to capture the high-frequency response of the point mobility of an infinite Timoshenko beam [10]

$$c_{oj,z} = 2A_r\sqrt{0.4G_r\rho_r} \quad j = 1 \sim 4 \tag{12}$$

where G_r is the shear modulus of the rail when Poisson's ratio of 0.3 is considered and ρ_r is the material density.

3.1.2. Parameters in the lateral direction

The lateral rail pad stiffness for the co-running track model can be calculated following the same procedure introduced in Section 3.1.1 but with rail lateral bending stiffness ($E_r I_{ry}$). However, the lateral equivalent ballast lateral stiffness is calculated by multiplying the length of the sleeper with the ballast lateral stiffness per unit length from the FE model, as shown in Equation (13).

$$k_{b,y} = s_{b,h}L_t \tag{13}$$

where $s_{b,h}$ is the ballast lateral stiffness per unit length and L_t is the length of the sleeper. Only one lateral spring-dashpot is modelled on each sleeper for the co-running track model, as shown in Figure 3, because the whole sleeper tends to move rigidly in the lateral direction.

As shown in Figure 1(c), the lateral stiffness for all rails gradually increases along the turnout, due to the increasing length of each sleeper, which consequently increases the resistance between the sleeper and the foundation. This increasing stiffness is modelled by a factor Δ_y, as defined in Equation (15) similar to the factor defined in Equation (11) for the vertical direction. This factor is the ratio of lateral stiffness of switch rail support obtained from the FE turnout model to the lateral stiffness, as given by Equation (2) based on the nominal sleeper length of 2.5 m. The equivalent lateral track parameters are calculated from stock rail parameters by multiplying the factor Δ_y. The increasing lateral stiffness, found in the FE model, can be approximated as a linear equation varying with respect to the distance from the switch toe, as defined in Equation (14) and the factor Δ_y determined from Equation (15).

$$K_{sh} = 1.1 * 10^5 x + 2.9 * 10^7 \tag{14}$$

$$\Delta_y = K_{sh}/K_{st} \tag{15}$$

Note here, the equivalent lateral ballast stiffness used in the MBS co-running track model is the overall lateral stiffness for one sleeper, which would be twice the lateral stiffness obtained from the FE turnout model. Furthermore, to obtain better agreement with the response at lower frequencies, instead of using the same value as the rail pad lateral stiffness, the parallel stiffness ($k_{0j,y}$) is 5 times higher than the lateral rail pad stiffness.

3.2. Mass properties

The mass for different bodies in the co-running track can also be calculated by taking into account the effective lengths, as shown from Equations (16)–(19).

$$\text{Rail mass} \quad m_r = A_r \rho_r L_{eff,r}/L_s \tag{16}$$

$$\text{Switch rail mass} \quad m_r = A_r \rho_r L_{eff,r} \Delta_z/L_s \tag{17}$$

$$\text{Sleeper mass} \quad m_t = A_s \rho_s L_t L_{eff,r} \Delta_y/L_s \tag{18}$$

$$\text{Sleeper mass at the crossing} \quad m_t = A_s \rho_s L_{eff,s} L_{eff,r}/L_s \tag{19}$$

The switch rail and sleeper builds up mass while travelling from switch toe towards crossing. This is factored by the variables Δ_z and Δ_y in Equations (17) and (18), respectively. The mass values for each component vary along the track. Furthermore, two different mass values would be derived for each component in the vertical and lateral directions due to different bending stiffnesses.

However, space-dependent mass variation and different mass distributions in two directions are not considered in the present work because the MBS software Simpack restricts mass to be constant in both vertical and lateral directions during a simulation. Because of this limitation, the simulation is divided into three zones, as shown in Figure 1, and the masses are assumed constant based on the vertical bending stiffness within each zone. In a future study, we could look into discretising the turnout into many more zones and calculate the improvement in the results. Finally, the three-layered co-running track properties for the whole turnout during three different simulation zones can be found in Table 2.

3.3. Validation by rail receptance

The parameters in Table 2 are used for the co-running MBS track model. Rail receptances of the two- and three-layered models are compared with the results from the complete FE turnout model, as shown in Figures 5 and 6 for the vertical and lateral directions, respectively. Rail receptance results from the MBS track model along the whole turnout have been compared with the results from the FE model. Only results at the most crucial locations, where the load is transferring at the switch and crossing, are shown in Figures 5 and 6, respectively.

Results from the two-layered MBS track model show a good agreement up to around 125 Hz in both directions, for both switch and crossing rail, but there are significant differences at higher frequencies. Although the three-layered MBS track model is not able to capture the detail of the pin-pin resonance, it shows a far better agreement against to the FE model up to 2000 Hz. Hence we consider that the three-layered MBS track model is a better approximation of the complete finite element model of the turnout.

4. Vehicle/turnout interaction

The Manchester benchmark vehicle [11] is run over the track and its foundation is under study. As mentioned in Figure 1, there are three simulation zones in the turnout. The first zone starts before the switch toe and extends until the crossing region. The second zone covers the crossing region, and the third covers a small portion of the plain track after that.

Table 2. Three-layer track properties for the present co-running track.

Parameter (and units)	Simulation-1 ($x < 44.29$ m)	Simulation-2 ($44.29 < x < 51.52$ m)	Simulation-3 ($x > 51.52$ m)	Equivalent formula
Vertical properties				
$k_{01,z}$ (N/m)	369×10^6	369×10^6	369×10^6	Same as $k_{rt1,z}$
$c_{01,z}$ (Ns/m)	315×10^3	315×10^3	315×10^3	Equation (12)
$k_{02,z}$ (N/m)	$369 \times 10^6\ \Delta_z$	$448 \times 10^6 – 453 \times 10^6$	448×10^6	Same as $k_{rt2,z}$
$c_{02,z}$ (Ns/m)	315×10^3	946×10^3	315×10^3	Equation (12)
$k_{03,z}$ (N/m)	369×10^6	369×10^6	369×10^6	Same as $k_{rt3,z}$
$c_{03,z}$ (Ns/m)	315×10^3	315×10^3	315×10^3	Equation (12)
$k_{04,z}$ (N/m)	369×10^6	369×10^6	369×10^6	Same as $k_{rt4,z}$
$c_{04,z}$ (Ns/m)	315×10^3	315×10^3	315×10^3	Equation (12)
$k_{rt1,z}$ (N/m)	369×10^6	369×10^6	369×10^6	Equation (6) with $E_r l_{r,z}$
$c_{rt1,z}$ (Ns/m)	77×10^3	77×10^3	77×10^3	Equation (7) with $E_r l_{r,z}$
$k_{rt2,z}$ (N/m)	$369 \times 10^6\ \Delta_z$	$448 \times 10^6 – 453 \times 10^6$	448×10^6	Equations (6) and (11) with $E_r l_{r,z}$
$c_{rt2,z}$ (Ns/m)	$77 \times 10^3\ \Delta_z$	94×10^3	93×10^3	Equations (7) and (11) with $E_r l_{r,z}$
$k_{rt3,z}$ (N/m)	369×10^6	369×10^6	369×10^6	Equation (6) with $E_r l_{r,z}$
$c_{rt3,z}$ (Ns/m)	77×10^3	77×10^3	77×10^3	Equation (7) with $E_r l_{r,z}$
$k_{rt4,z}$ (N/m)	369×10^6	369×10^6	369×10^6	Equation (6) with $E_r l_{r,z}$
$c_{rt4,z}$ (Ns/m)	77×10^3	77×10^3	77×10^3	Equation (7) with $E_r l_{r,z}$
$k_{tg1,z}$ (N/m)	$77 \times 10^6\ \Delta_z$	$93 \times 10^6 – 134 \times 10^6$	93×10^6	Equations (8) and (11) with $E_r l_{r,z}$
$c_{tg1,z}$ (Ns/m)	$77 \times 10^4\ \Delta_z$	$93 \times 10^4 – 134 \times 10^4$	93×10^4	Equations (9) and (11) with $E_r l_{r,z}$
$k_{tg2,z}$ (N/m)	77×10^6	77×10^6	77×10^6	Equation (8) with $E_r l_{r,z}$
$c_{tg2,z}$ (Ns/m)	77×10^4	77×10^4	77×10^4	Equation (9) with $E_r l_{r,z}$
Lateral properties				
$k_{01,y}$ (N/m)	$280 \times 10^6\ \Delta_y$	$280 \times 10^6\ \Delta_y$	$280 \times 10^6\ \Delta_y$	$5k_{rt1,y}$
$c_{01,y}$ (Ns/m)	315×10^3	315×10^3	315×10^3	Equation (12)
$k_{02,y}$ (N/m)	$280 \times 10^6\ \Delta_y$	265×10^6	$280 \times 10^6\ \Delta_y$	$5k_{rt2,y}$
$c_{02,y}$ (Ns/m)	315×10^3	946×10^3	315×10^3	Equation (12)
$k_{03,y}$ (N/m)	$280 \times 10^6\ \Delta_y$	1075×10^6	$280 \times 10^6\ \Delta_y$	$5k_{rt3,y}$
$c_{03,y}$ (Ns/m)	315×10^3	315×10^3	315×10^3	Equation (12)
$k_{04,y}$ (N/m)	$280 \times 10^6\ \Delta_y$	$280 \times 10^6\ \Delta_y$	$280 \times 10^6\ \Delta_y$	$5k_{rt4,y}$
$c_{04,y}$ (Ns/m)	315×10^3	315×10^3	315×10^3	Equation (12)
$k_{rt1,y}$ (N/m)	$56 \times 10^6\ \Delta_y$	$56 \times 10^6\ \Delta_y$	$56 \times 10^6\ \Delta_y$	Equations (15) and (6), with $E_r l_{r,y}$

(continued)

Table 2. Continued.

| Parameter (and units)	Simulation-1 ($x < 44.29$ m)	Simulation-2 ($44.29 < x < 51.52$ m)	Simulation-3 ($x > 51.52$ m)	Equivalent formula
$c_{rt1,y}$ (Ns/m)	$22 \times 10^3 \, \Delta_y$	$22 \times 10^3 \, \Delta_y$	$22 \times 10^3 \, \Delta_y$	Equations (15) and (7), with $E_r l_{r,y}$
$k_{rt2,y}$ (N/m)	$56 \times 10^6 \, \Delta_y$	53×10^6	$56 \times 10^6 \, \Delta_y$	Equations (15) and (6), with $E_r l_{r,y}$
$c_{rt2,y}$ (Ns/m)	$22 \times 10^3 \, \Delta_y$	21×10^3	$22 \times 10^3 \, \Delta_y$	Equations (15) and (7), with $E_r l_{r,y}$
$k_{rt3,y}$ (N/m)	215×10^6	215×10^6	215×10^6	Equations (15) and (6), with $E_r l_{r,y}$
$c_{rt3,y}$ (Ns/m)	45×10^3	45×10^3	45×10^3	Equations (15) and (7), with $E_r l_{r,y}$
$k_{rt4,y}$ (N/m)	$56 \times 10^6 \, \Delta_y$	$56 \times 10^6 \, \Delta_y$	$56 \times 10^6 \, \Delta_y$	Equations (15) and (6), with $E_r l_{r,y}$
$c_{rt4,y}$ (Ns/m)	$22 \times 10^3 \, \Delta_y$	$22 \times 10^3 \, \Delta_y$	$22 \times 10^3 \, \Delta_y$	Equations (15) and (7), with $E_r l_{r,y}$
$k_{tg,y}$ (N/m)	$56 \times 10^6 \, \Delta_y$	86×10^6	$56 \times 10^6 \, \Delta_y$	Equations (15) and (8), with $E_r l_{r,y}$
$c_{tg,y}$ (Ns/m)	$56 \times 10^4 \, \Delta_y$	86×10^4	$56 \times 10^4 \, \Delta_y$	Equations (15) and (9), with $E_r l_{r,y}$
Masses				
m_0 (kg)	2.5	2.5	2.5	
m_t (kg)	500	881	500	Equation (18) or Equation (19) with $E_r l_{r,z}$
m_{r1} (kg)	111	111	111	Equation (16) with $E_r l_{r,z}$
m_{r2} (kg)	111	409	111	Equation (16) with $E_r l_{r,z}$
m_{r3} (kg)	111	111	111	Equation (16) with $E_r l_{r,z}$
m_{r4} (kg)	111	111	111	Equation (16) with $E_r l_{r,z}$
J_t (kgm^2)	265	1213	265	$m_t(L_t^2 + h_t^2)/12$
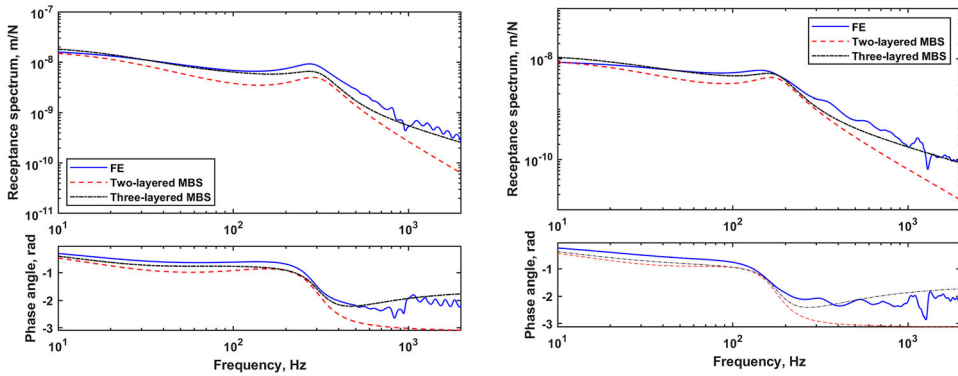
Figure 5. Vertical rail receptance at the crossing panel; (a) switch rail; (b) crossing rail.
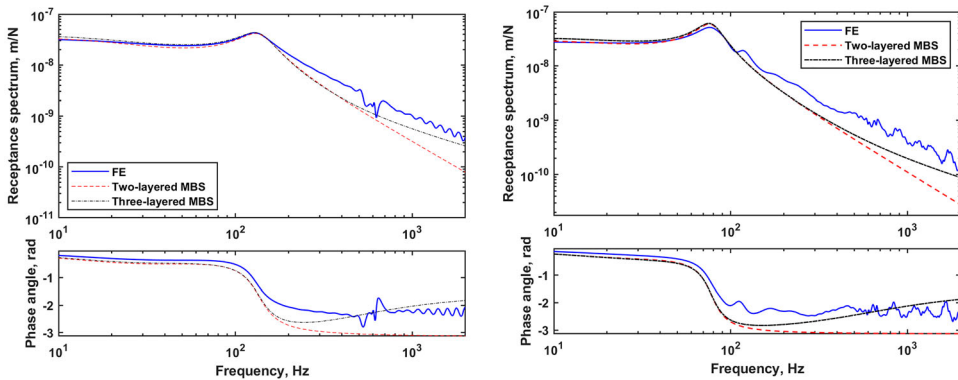

Figure 6. Lateral rail receptance at the crossing panel; (a) switch rail; (b) crossing rail.

Table 3. Location of different simulation zones and active rail bodies.

Simulation zone	Zone 1	Zone 2	Zone 3
[Start, End] in metres with reference to switch toe position	[−5, 44.29]	[44.29, 51]	[51, 60]
Active rail bodies	mr1 (stock), mr2 (switch), mr4 (stock)	mr1 (stock), mr2 (crossing), mr3 (check), mr4 (stock)	mr1 (stock), mr4 (stock)

4.1. Vehicle/turnout interaction model

The multi-body simulation executed in Simpack is a co-running track model. The mass of the rail body is kept constant within each of the three simulation regions, as mentioned previously. The stiffnesses and damping properties of the different force elements are continuously varied as a function of the rail position in the running direction. Hence due to the limitations of the co-running set-up, the masses are only piecewise continuous in the turnout, whereas stiffness and damping values are continuously variable. Table 3 shows the three different simulation zones and those rail bodies as shown in Figure 3 which are activated within each zone.
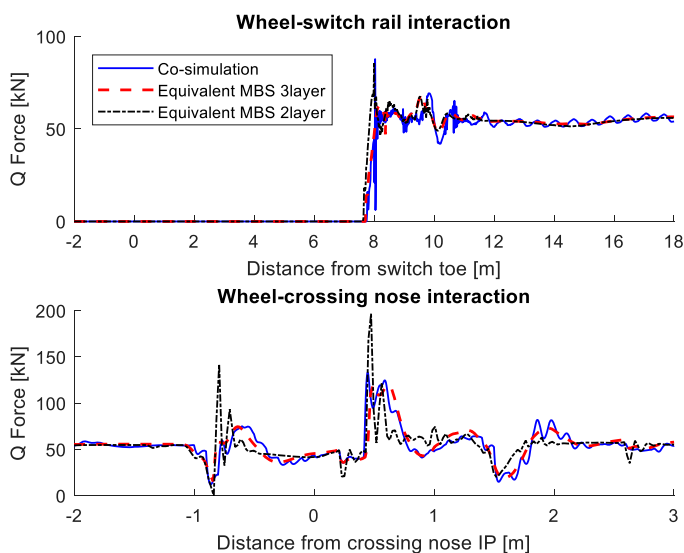
Figure 7. Comparing vertical contact forces at switch and crossing nose in through route.

The used software considers multiple contact patches between each wheel of the vehicle and the rail. To avoid singularity issues when the wheel jumps between different contact points, the software calculates the contact normal forces by means of an elastic approach, using parallel spring/damper elements. The spring force uses the penalty, or penetration method, which allows a realistic simulation of wheel lift and regain of contact.

4.2. Numerical results

The contact forces between the rail and the right wheel of the front most axle in the train are given in Figures 7 and 8. One of the signals in these figures is from [2], where the FE turnout model is coupled with the MBS vehicle model as a co-simulation analysis. Experimental data are not available for this vehicle–track interaction, hence the co-simulation is considered as the benchmark here as it directly employs the flexible turnout model, from which the parameters of the MBS model are derived. The vertical and lateral forces are presented as the vehicle passes through the switch rail and crossing nose. As seen from these forces, the two-layer equivalent MBS model oscillates more because of non-consideration of the appropriate rail damping in the track system. This is overcome by the three-layer MBS model, which also represents the FE model better in a wider frequency range, as shown in Figures 5 and 6. The results indicate that the equivalent MBS model could reproduce the same signals as the co-simulation.

As can be seen in Figures 7 and 8, all three models agree well in representing the overall trend of the contact forces. The results from the two-layered track model achieve a good agreement in both through route and diverging route with different train speeds in the switch region. But it overestimates the peak impact forces at the crossing panel despite a lower vehicle speed. This is due to the high-frequency nature of impacts at the crossing, which could not be estimated by the two-layered model. The three-layered MBS track model is able to give better agreement for both circumstances. With only 8
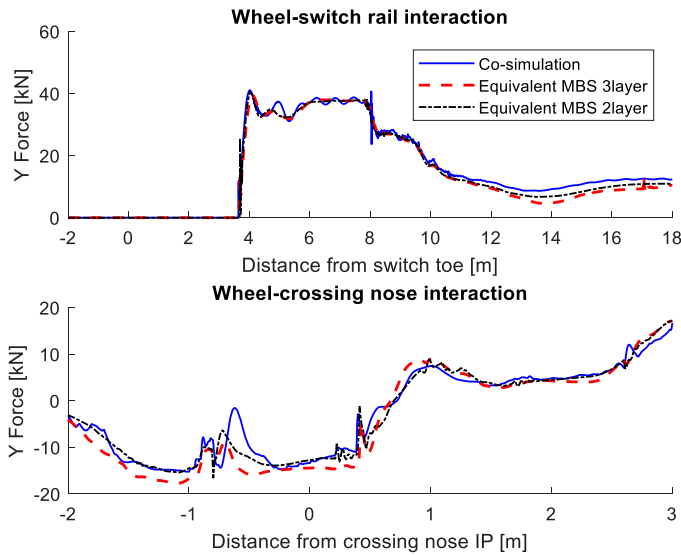
Figure 8. Comparing lateral contact forces at switch and crossing in diverging route.

more degrees of freedom compared to the two-layered model, the computational time increases by 10%. Despite this marginal increase in computational effort, this model can be preferred because of the significant benefits it offers in terms of accuracy at higher frequencies.

5. Conclusion

An efficient vehicle/turnout interaction model is presented which can capture the dynamic behaviour of a complete flexible turnout up to 2000 Hz. The paper presented the method to create a MBS model based on a detailed finite element model of the switch and crossing with its foundation. A two-layered simplified MBS model, commonly used in the literature, was initially assumed, for which the parameters were estimated out of the FE model. To improve the accuracy at higher frequencies, an additional layer of masses was included, and their parameters were also estimated. The degree of fit between the two equivalent MBS models with the parent FE model was qualitatively compared with the help of receptance plots in the frequency domain.

A vehicle is run over the two different models in both the straight and the divergent routes. The results from the presented MBS models have been compared with those from the FE/MBS co-simulation approach. Although the two models prove to be good approximation, the three-layered model proved itself to be far superior in correctly representing the peak force values better at the crossing region. Although the two-layered track model can model vehicle/turnout interaction for the switch region, the authors believe that the three-layered MBS track model offers significant benefits for use in the prediction of wheel–rail interactions through S&C; it correctly captures the higher frequencies, while only marginally increasing the computation time (and effort).

Disclosure statement

No potential conflict of interest was reported by the author(s).

ORCID

Jou-Yi Shih 🄳 http://orcid.org/0000-0002-7834-2305
Ramakrishnan Ambur 🄳 http://orcid.org/0000-0003-0636-0894
Roger Dixon 🄳 http://orcid.org/0000-0001-6753-8006

References

[1] Bezin Y, Pålsson BA, Kik W, et al. Multibody simulation benchmark for dynamic vehicle-track interaction in switches and crossings: results and method statements (submitted to VSD).

[2] Pålsson BA, Ambur R, Shih JY, et al. A comparison of track modelling formulations for simulation of dynamic vehicle-track interaction in switches and crossings (submitted to VSD).

[3] Di Gialleonardo E, Braghin F, Bruni S. The influence of track modelling options on the simulation of rail vehicle dynamics. J Sound Vib. 2012;331:4246–4258.

[4] Shih JY, Kostovasilis D, Bezin Y, et al. Modelling options for ballast track dynamics. The 24th International Congress on Sound and Vibration, 2017 Jul 23–27; London, UK. 2017.

[5] Chaar N. Wheelset structural flexibility and track flexibility in vehicle-track dynamic interaction [doctoral thesis]. Rail Vehicles, KTH, TRITA AVE 2007:17. ISBN 978-91-7178-636-4, Stockholm, Sweden, 2007.

[6] Kassa E, Nielsen J. Dynamic interaction between train and railway turnout: full-scale field test and validation of simulation models. Veh Syst Dyn. 2008;46:521–534.

[7] Pålsson BA, Nielsen J. Dynamic vehicle–track interaction in switches and crossings and the influence of rail pad stiffness – field measurements and validation of a simulation model. Veh Syst Dyn. 2015;53(6):734–755.

[8] Li X, Nielsen J, Pålsson BA. Simulation of track settlement in railway turnout, journal. Veh Syst Dyn. 2014;52:421–439.

[9] Yang J, Thompson DJ, Takano Y. Characterizing wheel flat impact noise with an efficient time domain model. Noise Vib Mitig Rail Transp Syst. 2015;126:109–116.

[10] Ruge P, Birk C. A comparison of infinite Timoshenko and Euler–Bernoulli beam models on Winkler foundation in the frequency- and time-domain. J Sound Vib. 2007;304(3–5):932–947.

[11] Iwnicki S. Manchester benchmarks for rail vehicle simulation. Veh Syst Dyn. 1998;30(3–4): 295–313.